Spin waves in the bilayer van der Waals magnet CrSBr

Rob den Teuling [1,*] Ritesh Das,[1] Artem V. Bondarenko,[1,2] Elena V. Tartakovskaya [1,2,3] Gerrit E. W. Bauer [4,5] and Yaroslav M. Blanter [1]

[1]*Kavli Institute of Nanoscience, Delft University of Technology, Lorentzweg 1, 2628 CJ Delft, The Netherlands*
[2]*V. G. Baryakhtar Institute of Magnetism of the NAS of Ukraine, 36b Vernadsky Boulevard, 03142 Kiev, Ukraine*
[3]*Institute of Spintronics and Quantum Information, Faculty of Physics and Astronomy, Adam Mickiewicz University, Poznań, Uniwersytetu Poznańskiego 2, 61-614 Poznań, Poland*
[4]*WPI-AIMR & IMR & CSIS, Tohoku University, 2-1-1 Katahira, Sendai 980-8577, Japan*
[5]*Kavli Institute for Theoretical Sciences, University of the Chinese Academy of Sciences, Beijing 10090, China*

(Received 17 March 2025; revised 8 September 2025; accepted 6 October 2025; published 29 October 2025; corrected 15 December 2025)

We derive analytical expressions for the spin-wave frequencies and precession amplitudes in monolayer and antiferromagnetically coupled bilayer CrSBr under in-plane external magnetic fields. The analysis covers the antiferromagnetic, ferromagnetic, and canted phases, demonstrating that the spin-wave frequencies in all phases are tunable by the applied magnetic field. We discuss the roles of intra- and interlayer exchange interactions, triaxial anisotropy, and intralayer dynamic dipolar fields in controlling the magnetization dynamics.

DOI: 10.1103/w4xn-2yff

I. INTRODUCTION

Since the discovery of long-range magnetic ordering in CrI_3 [1] and $Cr_2Ge_2Te_6$ [2] in 2017, two-dimensional (2D) van der Waals (vdW) magnets have been considered promising for applications such as spintronic logic circuits [3]. These devices employ spin waves, or magnons, as information carriers that do not suffer from Ohmic losses inherent to electron charge transport. For a comprehensive review on spin-wave computing, see Ref. [4]. Subsequently, numerous 2D vdW magnetic materials have been identified. For example, Fe_3GeTe_2 [5] and VSe_2 [6] remain magnetic down to single atomic layers. Others have been discovered experimentally and/or predicted theoretically [7]. They include ferromagnets, antiferromagnets, and layered antiferromagnets [8]. Magnetism in these materials has been shown to be tunable through various external stimuli, such as electric fields [9,10], pressure [11,12], strain [13,14], and doping [15,16]. Furthermore, these materials display multiple magnetic phase transitions that are sensitive to external parameters. This versatility makes them strong candidates for flexible, low-power applications across various electronic and quantum computing platforms.

Magnetic order in the layered 2D vdW material CrSBr was predicted by Guo *et al.* [17] and has been confirmed by experiments (see, e.g., Ref. [18]). CrSBr has a tetragonal crystal lattice, unlike most 2D vdW magnets that are hexagonal. It is the first layered material found to exhibit in-plane ferromagnetic (FM) order in monolayers but antiferromagnetic (AFM) coupling between the layers, similar to synthetic antiferromagnets [19]. The AFM order with vanishing net magnetization is robust against weak magnetic stray fields [20]. The FM ordering in the layers and relatively weak AFM coupling leads to low spin-wave frequencies in the GHz regime. Mono- and bilayers of CrSBr are ideal for studying the excitation, manipulation, and detection of 2D magnons. The magnetic properties of monolayer [21] and bilayer [22] CrSBr, including effects of biaxial [23] and triaxial [24] anisotropy, and dipolar exchange [25] have been reported. A comprehensive study of the magnon dispersion and precession amplitudes, under intra- and interlayer coupling, triaxial anisotropy, and dynamic dipolar interactions, is still lacking.

Here we present analytical expressions for the spin-wave frequencies and precession amplitudes as functions of intra- and interlayer exchange coupling, triaxial anisotropy constant, dynamic dipolar interactions, and in-plane external fields. The paper is organized as follows. Section II develops the theoretical framework. We start from Hamiltonians for mono- and bilayers to derive effective fields for the linearized Landau-Lifshitz (LL) equation. In Secs. III and IV, we provide the frequencies and eigenvectors of spin waves in the mono- and bilayer, respectively, as a function of in-plane external magnetic fields along the principal axes. Section V summarizes the results.

II. THEORETICAL FRAMEWORK

A. Hamiltonian

Figure 1 shows a bilayer of CrSBr with a tetragonal unit cell and AA stacking along the y direction [26]. The magnetic moments of the Cr atoms in a monolayer lie in the ab plane. In a multilayer, the spins order in CrSBr in an A-type AFM ordering, in which ferromagnetic monolayers align along the b axis with alternating orientations. Bulk CrSBr has a Néel temperature of 137 K [27], while the monolayer is ferromagnetic below 146 K [28]. In CrSBr, the dipolar field appears to be of the same order of magnitude as the magnetocrystalline anisotropy [29].

*Contact author: r.denteuling@tudelft.nl

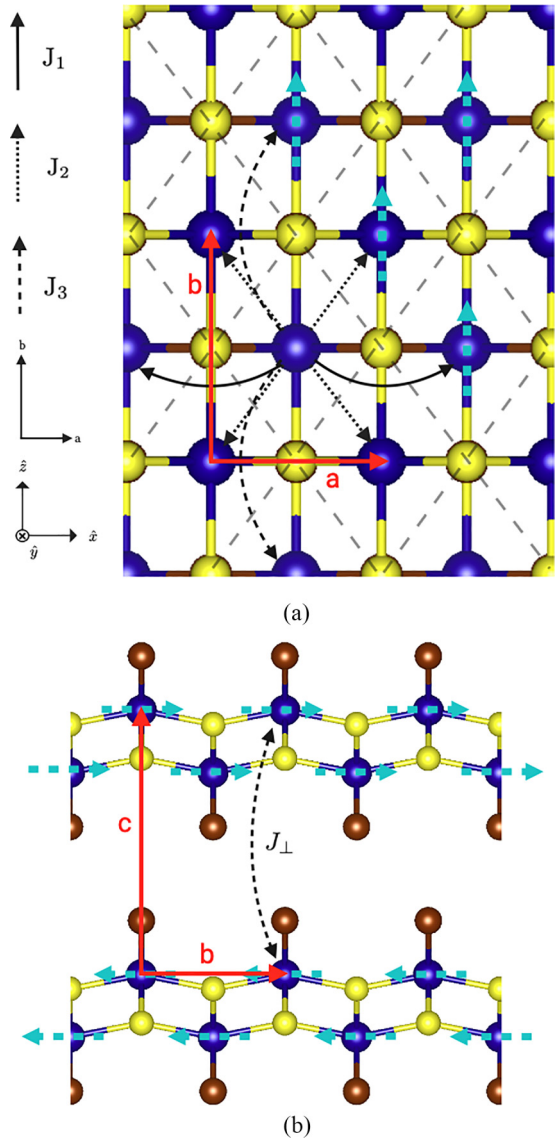

FIG. 1. Top (a) and side (b) views of bilayer CrSBr, illustrating the axes, lattice vectors, and exchange coupling constants J_i. Thin dashed lines indicate the primitive unit cell. The thick dashed arrows illustrate the magnetic moment orientations and AFM order. Chromium atoms are represented in blue, sulfur atoms are represented in yellow, and bromine atoms are represented in brown.

CrSBr is predicted to exhibit a triaxial anisotropy that favors spins to lie in the plane with a favored b direction, with strong intralayer FM coupling and weak interlayer AFM coupling [22]. Three coupling strengths dominate the intralayer exchange, viz., $\mathcal{J}_3 > \mathcal{J}_1 > \mathcal{J}_2 > 0$ (see Fig. 1), while the AFM interlayer exchange coupling $\mathcal{J}_\perp < 0$. The intralayer coupling constants of the two atoms in the unit cell (Appendix A) are not necessarily the same [27] but are assumed here to be equal. This simplifies the analytical treatment since the unit cell contains effectively only one chromium spin. The Brillouin zone is then twice as large without optical intralayer modes. We discuss this approximation in Appendix A for the monolayer and Appendix B for the bilayer.

TABLE I. Numerical values of the in-plane lattice constants a and b, the exchange constants $\mathcal{J}_i$ [13], and the anisotropy constants $\mathcal{D}_i$ [22].

a	3.54	10^{-10} m
b	4.73	10^{-10} m
$\mathcal{J}_1$	3.54	meV
$\mathcal{J}_2$	3.08	meV
$\mathcal{J}_3$	4.15	meV
$\mathcal{J}_\perp$	−15.5	μeV
$\mathcal{D}_x$	−12	μeV
$\mathcal{D}_y$	−78	μeV
$\mathcal{D}_z$	0	μeV

Parameter values for CrSBr vary across the literature [17,27,30,31]. Table I summarizes the numerical values used in this work. Seeing as experimental values are unavailable for the monolayer, we adopt the parameters from density functional theory (DFT). The intralayer exchange coupling constants are taken from Ref. [13] and the magnetic anisotropy constants from Ref. [22], where the sign of the anisotropy constants is changed to remain consistent with our choice of Hamiltonian. For the interlayer exchange coupling, we prefer the experimental value $\mathcal{J}_\perp = -15.5$ μeV [32] with a modulus that is an order of magnitude larger than the estimate from DFT [22]. Both the spin-orbit coupling and the shape anisotropy originating from dipole-dipole interactions contribute to the total magnetic anisotropy of monolayer CrSBr [22]. In the ground state, the second term dominates. Finally, the magnetic flux density of the CrSBr monolayer is $\mu_0 M_s = 0.48$ T [8,33]. The Hamiltonian for a bilayer is as follows:

$$H_{Bi} = H_A + H_B + H_{\text{int}}, \tag{1}$$

where H_A and H_B are the Hamiltonians for the isolated monolayers A and B, respectively. They include the Zeeman energy from the external field $\vec{B}_0$ (H_{Ext}), the intralayer exchange coupling (H_{Ex}), and magnetic anisotropy (H_{An}) [34]. Without dipolar interactions (see below),

$$H_A = \underbrace{-\sum_j \gamma\hbar\vec{B}_0\cdot\vec{S}_{j,A}}_{H_{\text{Ext}}} \underbrace{-\sum_{j,\sigma}\mathcal{J}_\sigma\vec{S}_{j,A}\cdot\vec{S}_{j+\sigma,A}}_{H_{\text{Ex}}} \underbrace{-\sum_j\left[\mathcal{D}_x S^2_{x,j,A}+\mathcal{D}_y S^2_{y,j,A}+\mathcal{D}_z S^2_{z,j,A}\right]}_{H_{\text{An}}}, \tag{2}$$

where j counts the local spins and σ sums over the nearest neighbors of the jth spin, γ is the gyromagnetic ratio, g is the Landé g factor, and μ_B is the Bohr magneton. The intralayer exchange coupling constants are denoted by $\mathcal{J}_\sigma$ as in Fig. 1, with

$$\mathcal{J}_{\pm\vec{a}} = \mathcal{J}_1, \quad \mathcal{J}_{\pm\vec{d}_1} = \mathcal{J}_{\pm\vec{d}_2} = \mathcal{J}_2, \quad \mathcal{J}_{\pm\vec{b}} = \mathcal{J}_3, \tag{3}$$

where $\vec{d}_1 = \frac{1}{2}(\vec{a}+\vec{b})$ and $\vec{d}_2 = \frac{1}{2}(\vec{a}-\vec{b})$. The Hamiltonian of layer B is written by making the substitution $A \rightleftharpoons B$.

The exchange interaction between the layers

$$H_{\rm int} = -\sum_j \mathcal{J}_\perp \vec{S}_{j,A} \cdot \vec{S}_{j,B} \tag{4}$$

is antiferromagnetic since $J_\perp < 0$.

We address the spin dynamics by making a classical approximation that allows us to write the equations of motion of the magnetization as a torque or LL equation [35,36],

$$\frac{d\vec{m}_j(t)}{dt} = -\gamma[\vec{m}_j(t) \times \vec{B}_{\rm eff}], \tag{5}$$

where $\vec{m}_j(t) = \gamma\hbar\vec{S}_j/M_s$, the normalized magnetic moment at a lattice site j on layer A or B, and $\vec{B}_{\rm eff}$ is the effective magnetic field that is the functional derivative [37],

$$\vec{B}_{\rm eff} = -\frac{1}{M_s}\frac{\partial\varepsilon}{\partial\vec{m}_l}, \tag{6}$$

of the energy density per unit cell ε that follows from the Hamiltonian by replacing the quantum spin operators by classical magnetization amplitudes via $\vec{S} = \vec{M}/(\gamma\hbar)$:

$$\begin{aligned}\varepsilon = &-M_s \sum_{l,\sigma} \frac{\mathcal{J}_\sigma S}{\gamma\hbar}\vec{m}_l \cdot \vec{m}_{l,\sigma} \\ &- M_s \sum_l \left(\frac{\mathcal{D}_x S}{\gamma\hbar}m_{x,l}^2 + \frac{\mathcal{D}_y S}{\gamma\hbar}m_{y,l}^2 + \frac{\mathcal{D}_z S}{\gamma\hbar}m_{z,l}^2\right) \\ &- M_s \sum_l \vec{B}_0 \cdot \vec{m}_l,\end{aligned} \tag{7}$$

where l runs over all sites in the unit cell and $S = M_s/(\gamma\hbar)$. We linearize the LL equation by the spin-wave ansatz

$$\begin{aligned}\vec{m}_l &= m_z\hat{z} + (m_x\hat{x} + m_y\hat{y})e^{i(\omega t - \vec{k}\cdot\vec{r}_l)} \\ &\equiv m_z\hat{z} + \underline{m}_x\hat{x} + \underline{m}_y\hat{y},\end{aligned} \tag{8}$$

where $\underline{m}_{x,y} = m_{x,y}e^{i(\omega t - \vec{k}\cdot\vec{r}_l)}$, in the small parameters $m_x, m_y \ll m_z = 1$.

The exchange coupling terms in the Hamiltonian lead to an effective field of the form $\vec{B}_{\rm Ex} = \alpha_i m_z\hat{z} + \beta_i\underline{m}_x\hat{x} + \beta_i\underline{m}_y\hat{y}$. Defining $J_k \equiv (\mathcal{J}_k S)/(\gamma\hbar)$, these terms read as follows:

$$\begin{aligned}&\alpha_1 = 2(J_1 + J_3), \quad \alpha_2 = 4J_2, \\ &\beta_1 = 2[J_1\cos(k_x a) + J_3\cos(k_z b)], \\ &\beta_2 = 2J_2\left[\cos\left(\tfrac{1}{2}k_x a + \tfrac{1}{2}k_z b\right) + \cos\left(\tfrac{1}{2}k_x a - \tfrac{1}{2}k_z b\right)\right].\end{aligned} \tag{9}$$

The anisotropy field reads

$$B_{{\rm An},\eta} = 2D_\eta\underline{m}_\eta, \quad D_\eta \equiv \mathcal{D}_\eta S/(\gamma\hbar), \quad \eta = x, y, z. \tag{10}$$

B. Dipolar fields

The dipolar interaction can be categorized into intralayer and interlayer contributions. Stamps [38] demonstrated that the dynamic dipolar *interlayer* interactions decay exponentially with distance. Furthermore, as we show elsewhere [39], in the case of bilayer CrSBr the product of the film thickness d and the wave vector k is numerically small and can be disregarded.

The continuum approximation significantly simplifies an analytical treatment of dipole-dipole interaction (Ewald) sums [40]. It is valid in the long-wave limit (small kd) and sufficiently accurate for larger k at which the exchange energy dominates. The tetragonal distortion induces a very small in-plane anisotropy in the static dipolar interaction energy [22] whose effect on the effective field we disregard.

The dipolar field in a thin film with in-plane magnetization along the z axis then reads [41,42]

$$\vec{B}_{\rm dip} = -\mu_0 M_s f(k) m_y\hat{y} - \mu_0 M_s\frac{k_x^2}{k^2}[1 - f(k)]m_x\hat{x}, \tag{11}$$

where

$$f(k) = \frac{1 - e^{-kd}}{kd}. \tag{12}$$

The thickness d of a vdW atomic monolayer is, strictly speaking, not well defined since it depends on the chemical bonds between the Cr, S, and Br atoms (Fig. 1). However, its main role is to regulate a divergence in the dipolar Ewald sum in strictly two dimensions. The numerical results are not very sensitive to deviations from our choice $d = b/2$. In the following, we add the intralayer dipolar fields [Eq. (11)] to $\vec{B}_{\rm eff}$.

III. MONOLAYER

Our results for the equilibrium state and the ferromagnetic resonance (FMR) frequency of the monolayer agree with the existing literature [23,24,34]. Here, we focus on the equilibrium and excited magnetization with an external magnetic field applied along the a and b axes. Substituting the effective fields into Eq. (5) leads to a 2×2 eigenvalue problem in the $[m_x, m_y]^T$ basis.

When the external field is applied along the easy axis, the eigenvalue problem and frequency dispersion (in Hz) of the lowest mode across the Brillouin zone (BZ) are

$$\omega\begin{bmatrix}m_x\\ m_y\end{bmatrix} = \gamma\begin{bmatrix}0 & iA\\ -iB & 0\end{bmatrix}\begin{bmatrix}m_x\\ m_y\end{bmatrix}, \quad \omega_- = \frac{\gamma}{2\pi}\sqrt{AB}, \tag{13}$$

where

$$\begin{aligned}A &= B_0 + 2(D_z - D_y) + [\alpha_1 - \beta_1] + [\alpha_2 - \beta_2] \\ &\quad + \mu_0 M_s f(k), \\ B &= B_0 + 2(D_z - D_x) + [\alpha_1 - \beta_1] + [\alpha_2 - \beta_2] \\ &\quad + \mu_0 M_s\frac{k_x^2}{k^2}[1 - f(k)].\end{aligned} \tag{14}$$

The non-normalized eigenvector reads

$$\vec{m}_{\omega_-} = \begin{bmatrix}1\\ -i\sqrt{\frac{B}{A}}\end{bmatrix} \tag{15}$$

A magnetic field along the intermediate axis causes a canting of the sublattice spins in the a direction by an angle of $\theta = \arcsin[B_0/2(D_z - D_x)]$ from the easy axis. We linearize $\hat{e}_\gamma^A$ as explained in Appendix C. In the canted basis $[m_\alpha, m_\beta]^T$, the exchange field reads $\vec{B}_{\rm Ex} = \alpha_i m_\gamma\hat{e}_\gamma + \beta_i\underline{m}_\alpha\hat{e}_\alpha + \beta_i\underline{m}_\beta\hat{e}_\beta$ and the dipolar field is $\vec{B}_{\rm dip} = -\mu_0 M_s f(k)m_\beta\hat{e}_\beta - \mu_0 M_s\frac{k_\alpha^2}{k^2}[1 - f(k)]m_\alpha\hat{e}_\alpha$. The saturation field that fully aligns the magnetic moments along the intermediate axis is $B_{\rm sat} = 2(D_z - D_x)$.

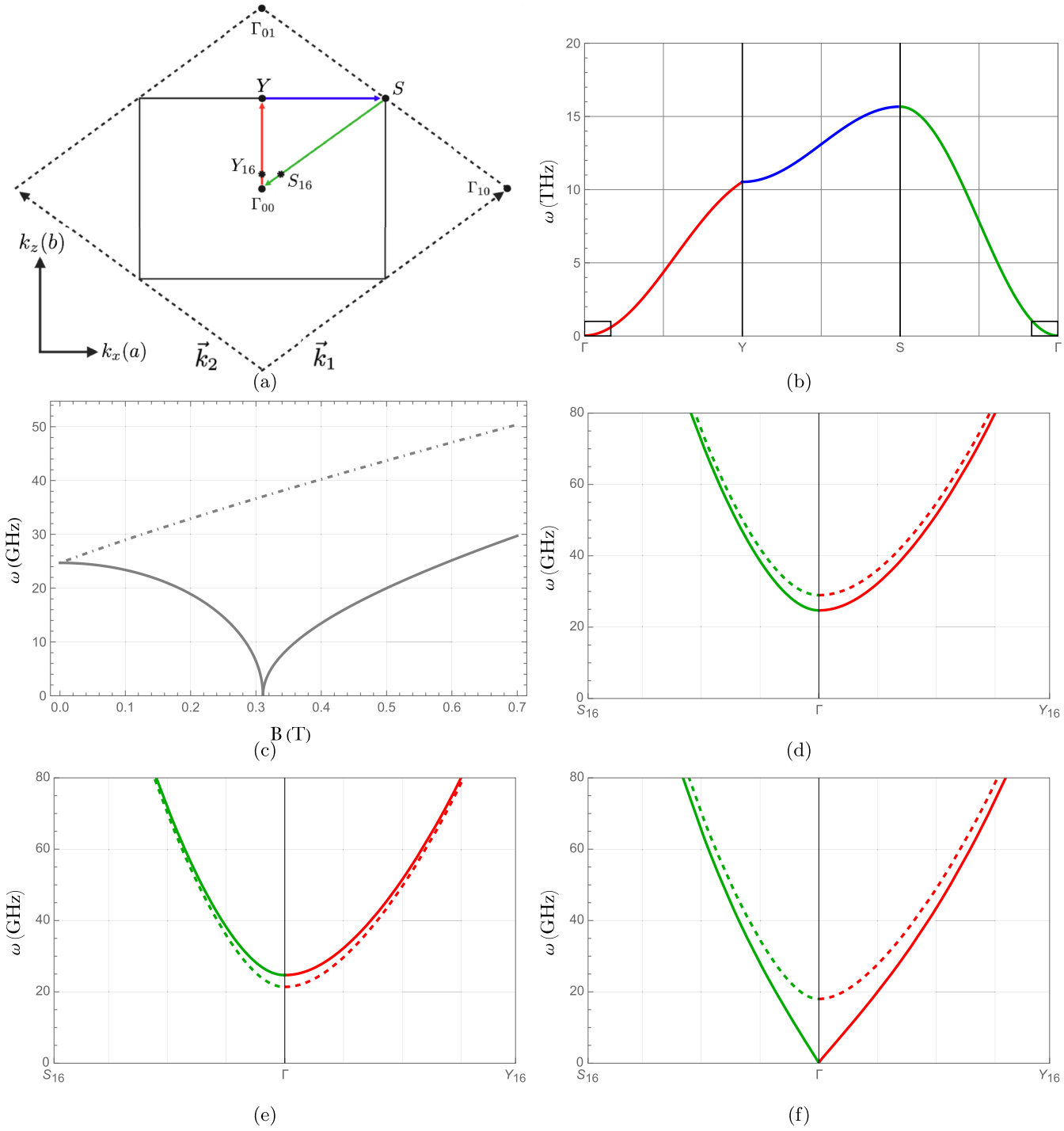

FIG. 2. (a) Brillouin zone (BZ) of the ferromagnetic monolayer CrSBr. The solid lines correspond to two inequivalent chromium atoms per monolayer unit cell, while the dashed lines indicate the BZ when the two chromium atoms are approximated to be equivalent. (b) Dispersion of monolayer CrSBr without applied magnetic field. The colors of the curve indicate the path in the BZ, while the small rectangles indicate the dispersions around the origin that are enlarged in panels (d)–(f). (c) Monolayer resonance frequencies ($k = 0$). The dash-dotted curve corresponds to an external magnetic field along the easy axis, and the solid curve is for a field along the intermediate axis (in-plane normal to the easy axis). (d)–(f) Monolayer dispersion relations close to the Γ point for two magnetic fields (dotted curves indicate higher fields). (d) External fields of 0 and $-\frac{1}{2}J_\perp$ along the easy axis. (e) External fields of 0 and $\frac{1}{2}B_{\text{sat}}$ along the intermediate axis. (f) External fields of B_{sat} and $\frac{3}{2}B_{\text{sat}}$ along the intermediate axis. B_{sat} is the critical field that fully aligns all spins.

The eigenvalue matrix and the frequency dispersion in the canted and saturated ($\theta = \pi/2$) phases are as follows:

$$\gamma\begin{bmatrix} 0 & iC \\ -iD & 0 \end{bmatrix}, \quad \omega_- = \frac{\gamma}{2\pi}\sqrt{CD}, \tag{16}$$

where

$$\begin{aligned} C &= B_0 \sin\theta + 2(D_x \sin^2\theta + D_z \cos^2\theta - D_y) \\ &\quad + [\alpha_1 - \beta_1] + [\alpha_2 - \beta_2] + \mu_0 M_s f(k), \\ D &= B_0 \sin\theta + 2(D_z - D_x)\cos(2\theta) \\ &\quad + [\alpha_1 - \beta_1] + [\alpha_2 - \beta_2] + \mu_0 M_s \frac{k_\alpha^2}{k^2}[1 - f(k)], \end{aligned} \tag{17}$$

with eigenvectors

$$\vec{m}_{\omega_-} = \begin{bmatrix} 1 \\ -i\sqrt{\frac{D}{C}} \end{bmatrix} \tag{18}$$

For fields applied along the intermediate axis, the saturation field at which the FMR frequency vanishes is $B_{\text{sat}} \approx 0.31$ T.

Figure 2(a) show the BZ of monolayer CrSBr [43] spanned by the reciprocal unit vectors $\vec{k}_1 = [2\pi/a \quad 2\pi/b]^T$ and $\vec{k}_2 = [-2\pi/a \quad 2\pi/b]^T$. The colored arrows show the path in the BZ used in plotting the dispersion. Figure 2(b) shows the magnon dispersion of a CrSBr monolayer in the absence of external magnetic fields. The effects of the magnetic crystal anisotropy and dipolar interactions are relatively small compared to that of the intralayer exchange, except for the small wave vector region close to the Γ point, as shown in the boxes of Fig. 2(b). Figure 2(c) shows the resonance frequencies and excited modes for the collinear and canted phases as a function of the applied field. Figures 2(d)–2(f) show the dispersion relations of the monolayer with external fields applied along the easy and intermediate axes. The red and green curves follow the $\Gamma_{00} \to Y_{16}$ and $\Gamma_{00} \to S_{16}$ paths, respectively, corresponding to 1/16th of the paths from Γ_{00} to the BZ boundary in Fig. 2(a). A field along the easy axis causes an upward shift of the entire spectrum with increasing field. A transverse field initially shifts the frequencies downwards until vanishing at B_{sat}, beyond which it increases monotonically with the field.

IV. BILAYER

We now turn to the magnetic properties of bilayer CrSBr in the presence of an external magnetic field applied along the easy and intermediate axes. In the basis

$$\begin{bmatrix} m_{\alpha,A} \\ m_{\alpha,B} \\ m_{\beta,A} \\ m_{\beta,B} \end{bmatrix}, \tag{19}$$

we have to solve an LL 4×4 matrix equation, where $\alpha = x$ ($\alpha = z$) when magnetic moments are collinear with the easy (intermediate) axis, respectively.

When external magnetic fields vanish, the ground state is an antiferromagnet with antiparallel orientation of the monolayer magnetizations [44]. Since the interlayer exchange field is weak, an external field along the easy axis induces spin-flip transition to a collinear ferromagnetic state at a critical field strength, B_{crit}, rather than a spin-flop transition observed in many other AFMs. In the following, we compute the equilibrium magnetization, frequency, and eigenvectors for an in-plane external magnetic field applied along the easy and intermediate axes. The FMR and antiferromagnetic resonance frequencies in bulk systems are known [23,24], the spin-wave dispersion and eigenvector spectra of the bilayer including the triaxial anisotropy and dipolar interactions are to our knowledge new.

A. Antiferromagnetic phase

The resonance frequencies for the AFM phase are found from the eigenvalue equation

$$\omega\begin{bmatrix} m_{x,A} \\ m_{x,B} \\ m_{y,A} \\ m_{y,B} \end{bmatrix} = \gamma\begin{bmatrix} 0 & 0 & iE_1 & -iJ_\perp \\ 0 & 0 & iJ_\perp & -iE_2 \\ -iF_1 & iJ_\perp & 0 & 0 \\ -iJ_\perp & iF_2 & 0 & 0 \end{bmatrix}\begin{bmatrix} m_{x,A} \\ m_{x,B} \\ m_{y,A} \\ m_{y,B} \end{bmatrix}, \tag{20}$$

where

$$\begin{aligned} E_1 &= B_0 + 2(D_z - D_y) + [\alpha_1 - \beta_1] + [\alpha_2 - \beta_2] \\ &\quad - J_\perp + \mu_0 M_s f(k), \\ E_2 &= -B_0 + 2(D_z - D_y) + [\alpha_1 - \beta_1] + [\alpha_2 - \beta_2] \\ &\quad - J_\perp + \mu_0 M_s f(k), \\ F_1 &= B_0 + 2(D_z - D_x) + [\alpha_1 - \beta_1] + [\alpha_2 - \beta_2] \\ &\quad - J_\perp + \mu_0 M_s \frac{k_x^2}{k^2}[1 - f(k)], \\ F_2 &= -B_0 + 2(D_z - D_x) + [\alpha_1 - \beta_1] + [\alpha_2 - \beta_2] \\ &\quad - J_\perp + \mu_0 M_s \frac{k_x^2}{k^2}[1 - f(k)]. \end{aligned} \tag{21}$$

The antisymmetry of the external field along the magnetic moments (terms E_1 and E_2, and F_1 and F_2) renders the analytical forms of the frequencies:

$$\omega_\mp = \frac{\gamma}{2\pi}\frac{1}{\sqrt{2}}\sqrt{E_1F_1 + E_2F_2 - 2J_\perp^2 \mp \sqrt{(E_1F_1 + E_2F_2 - 2J_\perp^2)^2 - 4(E_1E_2 - J_\perp^2)(F_1F_2 - J_\perp^2)}}. \tag{22}$$

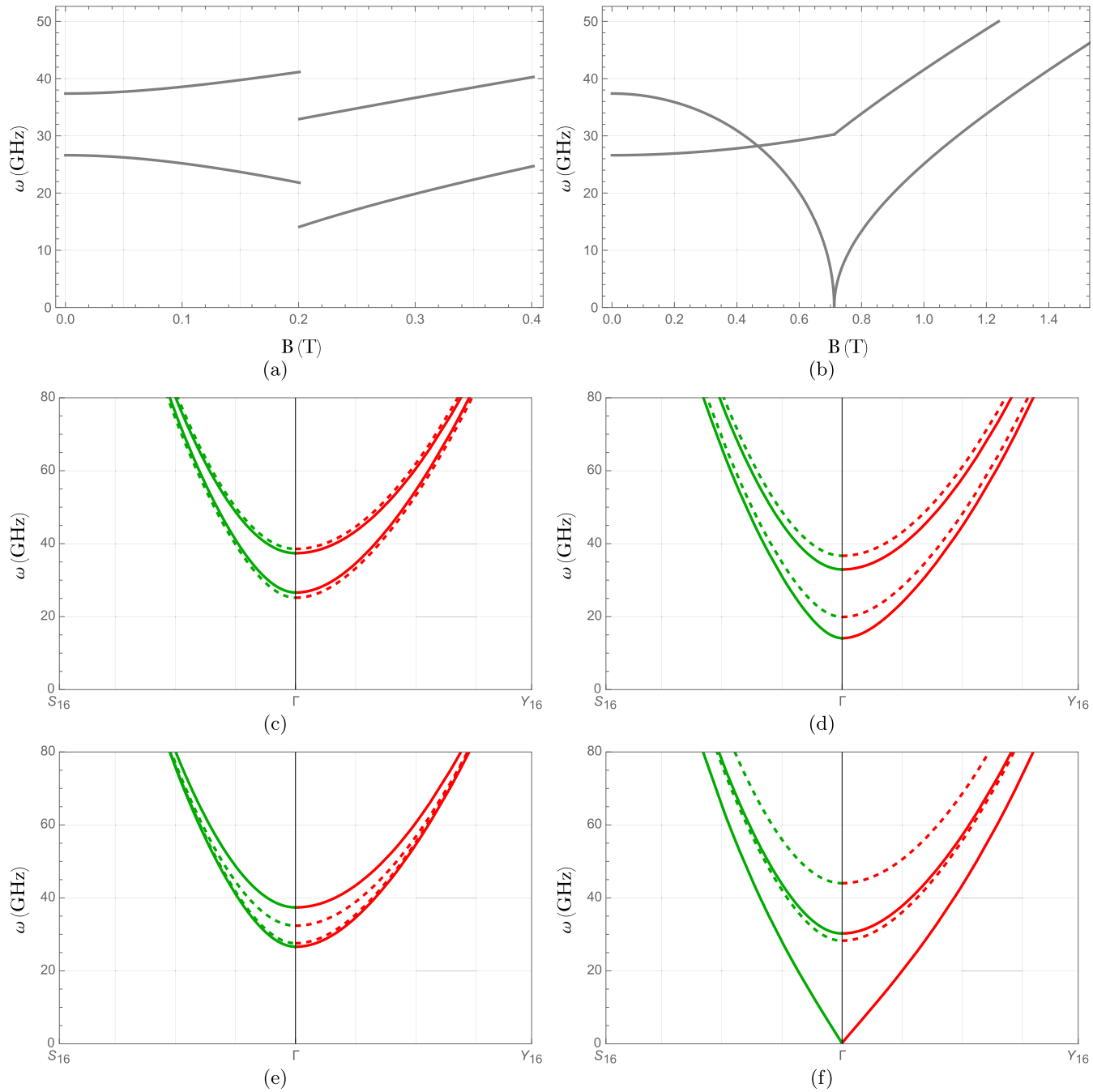

FIG. 3. (a), (b) Bilayer magnetic resonance frequencies ($k = 0$) as a function of the magnetic field. (a) AFM (left of the transition at $B_0 < B_c^{\text{flip}}$) and FM ($B_0 > B_c^{\text{flip}}$) phases for a field direction along the easy axis. (b) Canted ($B < B_{\text{sat}}^{\text{cant}}$) and saturated FM ($B > B_{\text{sat}}^{\text{cant}}$) phases for an in-plane field normal to the easy axis. (c)–(f) Bilayer dispersion relations close to the Γ point for two magnetic field strengths (dotted curves indicate higher fields). (c) $B_0 = 0$ and $B_0 = \frac{1}{2}B_{\text{crit}}^{\text{flip}}$ (dotted line) along the easy axis. (d) External fields of $B_0 = B_c^{\text{flip}}$ and $B_0 = \frac{3}{2}B_{\text{crit}}^{\text{flip}}$ along the easy axis, where $B_{\text{crit}}^{\text{flip}}$ aligns the spins ferromagnetically along the easy axis. (e) External fields of $B_0 = 0$ and $B_0 = \frac{1}{2}B_{\text{sat}}^{\text{cant}}$ along the intermediate axis. (f) External fields of $B_{\text{sat}}^{\text{cant}}$ and $\frac{3}{2}B_{\text{sat}}^{\text{cant}}$ along the intermediate axis. $B_{\text{sat}}^{\text{cant}}$ aligns the spins ferromagnetically along the intermediate in-plane normal-to-easy axis.

The two positive frequency branches correspond to the lower-frequency (β mode) and higher-frequency (α mode) excitations of the magnetic moments in the unit cell [34]. When D_x, D_y, and the dipolar interaction vanish, we recover the well-known result by Kittel [45].

B. Spin-flip phase

An external field along the easy axis induces a spin-flip transition from the AFM to FM configuration at a critical value $B_{\text{crit}}^{\text{flip}}$, as illustrated in Fig. 7 in Appendix D. The

equilibrium configuration minimizes the energy of Eq. (7) as a function of θ_A and θ_B, where $m_{x,i} = \cos\theta_i$ and $m_{z,i} = \sin\theta_i$, $i = A$ or B, and θ_i is the angle with the x axis. When $B_0 < B_{\text{crit}}^{\text{flip}}$, the ground state is an AFM state with $\theta_A = -\theta_B = \pi/2$, as discussed in Ref. [44]. When $B_0 \geqslant B_{\text{crit}}^{\text{flip}}$, $\theta_A = \theta_B = \pi/2$ minimizes the energy. By comparing the energies of AFM and FM states, we find $B_{\text{crit}}^{\text{flip}} = -J_\perp \approx 0.2\,\text{T}$ [32]. The eigenvalue matrix reads

$$\gamma \begin{bmatrix} 0 & 0 & iG & -iJ_\perp \\ 0 & 0 & -iJ_\perp & iG \\ -iH & iJ_\perp & 0 & 0 \\ iJ_\perp & -iH & 0 & 0 \end{bmatrix}, \tag{23}$$

and frequencies of the two modes are

$$\omega_\mp = \frac{\gamma}{2\pi}\sqrt{(G \mp J_\perp)(H \mp J_\perp)}, \tag{24}$$

where

$$\begin{aligned} G &= B_0 + 2(D_z - D_y) + [\alpha_1 - \beta_1] + [\alpha_2 - \beta_2] \\ &\quad + J_\perp + \mu_0 M_s f(k), \\ H &= B_0 + 2(D_z - D_x) + [\alpha_1 - \beta_1] + [\alpha_2 - \beta_2] \\ &\quad + J_\perp + \mu_0 M_s \frac{k_x^2}{k^2}[1 - f(k)], \end{aligned} \tag{25}$$

with eigenvectors

$$\vec{m}_{\omega_-} = \begin{bmatrix} 1 \\ 1 \\ i\sqrt{\frac{H-J_\perp}{G-J_\perp}} \\ i\sqrt{\frac{H-J_\perp}{G-J_\perp}} \end{bmatrix}, \quad \vec{m}_{\omega_+} = \begin{bmatrix} 1 \\ -1 \\ i\sqrt{\frac{H+J_\perp}{G+J_\perp}} \\ -i\sqrt{\frac{H+J_\perp}{G+J_\perp}} \end{bmatrix}. \tag{26}$$

As for the monolayer, we focus on the regime close to the Γ point. Figure 3(a) displays the resonance frequencies of the AFM and FM phases in a bilayer. At the spin-flip transition, both frequencies drop abruptly. In the FM phase, both mode frequencies increase again with the external field [34].

Figures 3(c) and 3(d) show the dispersion below and above the spin-flip transition, respectively. At $B_0 = B_{\text{crit}}^{\text{flip}}$, the frequencies are minimal and shift to higher values again with increasing field.

C. Canted phase

An external magnetic field applied along the intermediate axis leads to a canting of the layer magnetizations as illustrated in Fig. 8 in Appendix D that becomes a ferromagnet at the saturation value $B_{\text{sat}}^{\text{cant}}$. In the canted phase, the magnetic moments of the individual layers are noncollinear. The LL equation can best be solved in a sublattice-specific coordinate system described in Appendix C and linearized for small amplitudes around the equilibrium orientations $\hat{e}_\gamma^A$ and $\hat{e}_\gamma^B$. The intralayer dipolar fields, Eq. (11), in the respective bases are

$$\vec{B}_{\text{dip},i} = -\mu_0 M_s f(k) m_{\beta,i}\hat{e}_\beta^i - \mu_0 M_s \frac{k_{\alpha,i}^2}{k^2}[1 - f(k)]m_{\alpha,i}\hat{e}_\alpha^i, \tag{27}$$

where $i = A$ or B indicates the sublattice. In subsequent expressions, $k_{\alpha,i}^2$ can be written as a function of k_x and k_z via Eqs. (C2) and (C3). By minimizing the energy yields, on obtains the canting angle $\sin\theta = B_0/[2(D_z - D_x - J_\perp)]$. The resonance frequencies for the canted phase solve the LL equation

$$\omega \begin{bmatrix} m_{\alpha,A} \\ m_{\alpha,B} \\ m_{\beta,A} \\ m_{\beta,B} \end{bmatrix} = \gamma \begin{bmatrix} 0 & 0 & iI & -iJ_\perp \\ 0 & 0 & -iJ_\perp & iI \\ -iK_A & iK_1 & 0 & 0 \\ iK_1 & -iK_B & 0 & 0 \end{bmatrix} \begin{bmatrix} m_{\alpha,A} \\ m_{\alpha,B} \\ m_{\beta,A} \\ m_{\beta,B} \end{bmatrix}, \tag{28}$$

where

$$\begin{aligned} I &= B_0 \sin\theta + 2(D_x \sin^2\theta + D_z \cos^2\theta - D_y) \\ &\quad + [\alpha_1 - \beta_1] + [\alpha_2 - \beta_2] - J_\perp \cos(2\theta) + \mu_0 M_s f(k), \\ K_A &= B_0 \sin(\theta) + 2(D_z - D_x)\cos(2\theta) + [\alpha_1 - \beta_1] \\ &\quad + [\alpha_2 - \beta_2] - J_\perp \cos(2\theta) + \mu_0 M_s \frac{k_{\alpha,A}^2}{k^2}[1 - f(k)], \\ K_B &= B_0 \sin(\theta) + 2(D_z - D_x)\cos(2\theta) + [\alpha_1 - \beta_1] \\ &\quad + [\alpha_2 - \beta_2] - J_\perp \cos(2\theta) + \mu_0 M_s \frac{k_{\alpha,B}^2}{k^2}[1 - f(k)], \\ K_1 &= -J_\perp \cos(2\theta). \end{aligned} \tag{29}$$

The solutions read

$$\omega_\mp = \frac{\gamma}{2\pi}\frac{1}{\sqrt{2}}\sqrt{I(K_A + K_B) + 2J_\perp K_1 \mp \sqrt{[I(K_A + K_B) + 2J_\perp K_1]^2 - 4\big(I^2 - J_\perp^2\big)\big(K_A K_B - K_1^2\big)}}. \tag{30}$$

The analytical solutions for the eigenfrequencies and eigenvectors are cumbersome again, this time due to $k_{\alpha,A}^2 \neq k_{\alpha,B}^2$ for $0 < \theta < \frac{\pi}{2}$ (terms K_A and K_B).

At the saturation field $B_{\text{sat}}^{\text{cant}} = 2(D_z - D_x - J_\perp) \approx 0.71\,\text{T}$ and above, both layer magnetizations are parallel to the magnetic field direction. When $B_0 \geqslant 2(D_z - D_x - J_\perp)$, we set $\cos\theta = 0$ and $\sin\theta = 1$, so that the basis vector reads $[m_{z,A}, m_{z,B}, m_{y,A}, m_{y,B}]^T$, leading to the frequencies

$$\omega_\mp = \frac{\gamma}{2\pi}\sqrt{(L \mp J_\perp)(M \mp J_\perp)}, \tag{31}$$

where

$$L = B_0 + 2(D_x - D_y) + [\alpha_1 - \beta_1] + [\alpha_2 - \beta_2] + J_\perp + \mu_0 M_s f(k),$$
$$M = B_0 + 2(D_x - D_z) + [\alpha_1 - \beta_1] + [\alpha_2 - \beta_2] + J_\perp + \mu_0 M_s \frac{k_z^2}{k^2}[1 - f(k)], \tag{32}$$

with eigenvectors

$$\vec{m}_{\omega_-} = \begin{bmatrix} 1 \\ 1 \\ i\sqrt{\frac{M-J_\perp}{L-J_\perp}} \\ i\sqrt{\frac{M-J_\perp}{L-J_\perp}} \end{bmatrix}, \quad \vec{m}_{\omega_+} = \begin{bmatrix} 1 \\ -1 \\ i\sqrt{\frac{M+J_\perp}{L+J_\perp}} \\ -i\sqrt{\frac{M+J_\perp}{L+J_\perp}} \end{bmatrix}, \tag{33}$$

in the basis $[m_{z,A}, m_{z,B}, m_{y,A}, m_{y,B}]^T$. This solution is identical to the spin-flip FM phase after substituting $x \rightleftharpoons z$. Figure 3(b) illustrates the resonance frequencies for the canted (below $B_{\text{sat}}^{\text{cant}}$) and saturated (above $B_{\text{sat}}^{\text{cant}}$) phases of the bilayer. In the canted phase, we may expect a magnon Hanle effect at the mode crossing at $B_0 \approx 0.47$ T [46]. Figure 3(e) pictures the dispersion in the canted phase below saturation. Both bands decrease in energy for an increasing external field. Figure 3(f) shows the dispersion in the saturated phase. At $B_0 = B_{\text{sat}}^{\text{cant}}$, the lower band becomes soft, above which all frequencies increase monotonically with the applied field.

In all phases, for both the monolayer and the bilayer, inclusion of the dynamic dipolar field increases the frequency around the Γ point by ∼11%.

In Appendix E, we show that our results agree very well with numerical simulations by the program package SPINW [47].

The LL equations can also be derived from the leading term of the Holstein-Primakoff expansion of the spin Hamiltonian [48]. We made sure that the results for the magnon dispersion and eigenmodes were identical.

V. CONCLUSION

We derived spin-wave frequencies and eigenvectors from the linearized monolayer and bilayer CrSBr under in-plane magnetic fields including FM intralayer and AFM interlayer exchange couplings, triaxial magnetic anisotropy, intralayer dipolar interactions, and external magnetic fields along the easy and intermediate axes.

In principle, our approach applies to synthetic antiferromagnets and can be generalized to multilayer systems at the cost of losing closed analytic forms.

Our results highlight the tunability of spin-wave spectra in CrSBr through external magnetic fields and detail the interplay among the external field, inter- and intralayer exchange coupling, magnetic anisotropy, and dynamic dipolar interactions. They can be tested by magnetic resonance spectroscopy. They form the input to compute magnetic stray fields, propagating magnon spectroscopy, Hanle effects, and diffuse spin transport including magnon spin conductivities and spin Seebeck coefficients.

ACKNOWLEDGMENTS

This publication is part of the project "Ronde Open Competitie XL" (File No. OCENW.XL21.058) and "Ronde Open Competitie ENW Pakket 21-3" (File No. OCENW.M.21.215) which are (partly) financed by the Dutch Research Council (NWO). A.V.B. was supported by the EIC Pathfinder PALANTIRI Project. E.V.T. was supported by the National Science Center of Poland, Project No. UMO-2023/49/B/ST3/02920. G.E.W.B. was supported by JSPS Kakenhi Grants No. 22H04965 and No. JP24H02231. We thank Samer Kurdi and Fabian Gerritsma for insightful discussions. Images were made with BioRender and the crystallographic model was taken from VESTA.

DATA AVAILABILITY

The data that support the findings of this article are openly available [49].

APPENDIX A: TWO-SUBLATTICE MONOLAYER CrSBr

As discussed in the main text, the precise values of the intralayer exchange coupling parameters are not well known. Working with two slightly different couplings in the x and z directions could be better than the isotropic model used in the main text. Figure 4 illustrates the magnetic configuration with anisotropic exchange and two chromium atoms per unit cell. Compared to the isotropic exchange model the magnetic unit cell becomes twice as large. The number of magnon modes in a half as large Brillouin zone doubles. The analytical diagonalization of the corresponding 4×4 eigenvalue matrices for the monolayer is tedious and we do not show the lengthy solutions here.

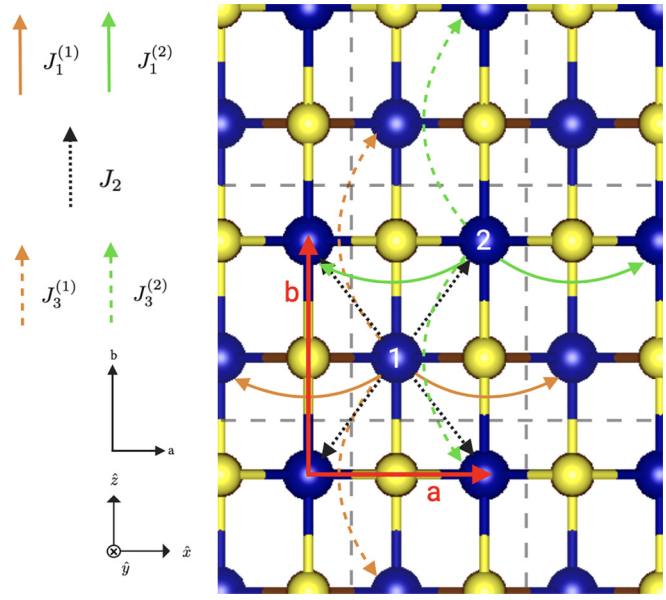

FIG. 4. Anisotropic intralayer exchange coupling constants.

The Hamiltonian for sublattice 1 in layer A for such a configuration reads

$$\begin{aligned}\hat{H}_A^{(1)} = &\underbrace{-\sum_{j,\sigma_1} \mathcal{J}_{\sigma_1} \vec{S}_{j,A}^{(1)} \cdot \vec{S}_{j+\sigma_1,A}^{(1)}}_{\hat{H}_{Ex,1}} \\ &\underbrace{-\sum_{j,\sigma_2} \mathcal{J}_{\sigma_2} \vec{S}_{j,A}^{(1)} \cdot \vec{S}_{j+\sigma_1,A}^{(1)}}_{\hat{H}_{Ex,2}} \\ &\underbrace{-\sum_{j} \left[\mathcal{D}_x S_{x,j,A}^{(1)2} + \mathcal{D}_y S_{y,j,A}^{(1)2} + \mathcal{D}_z S_{z,j,A}^{(1)2}\right]}_{\hat{H}_{\mathrm{An}}} \\ &\underbrace{-\sum_{j} \gamma \hbar \vec{B}_0 \cdot \vec{S}_{j,A}^{(1)}}_{\hat{H}_{\mathrm{Ext}}},\end{aligned} \tag{A1}$$

with

$$\begin{aligned} J_{\vec{\sigma}_{\pm a}}^{(1)} &= J_1^{(1)}, \\ J_{\vec{\sigma}_{\pm a}}^{(2)} &= J_1^{(2)}, \\ J_{\vec{\sigma}_{\pm d_1}} &= J_{\vec{\sigma}_{\pm d_2}} = J_2, \\ J_{\vec{\sigma}_{\pm b}}^{(1)} &= J_3^{(1)}, \\ J_{\vec{\sigma}_{\pm b}}^{(2)} &= J_3^{(2)}, \end{aligned} \tag{A2}$$

where $\vec{d}_1 = \frac{1}{2}(\vec{a} + \vec{b})$ and $\vec{d}_2 = \frac{1}{2}(\vec{a} - \vec{b})$, so that

$$\begin{aligned} \alpha_1^{(1)} &= 4\left(J_1^{(1)} + J_3^{(1)}\right), \\ \beta_1^{(1)} &= 4\left[J_1^{(1)} \cos(k_x a) + J_3^{(1)} \cos(k_z b)\right], \\ \alpha_1^{(2)} &= 4\left(J_1^{(2)} + J_3^{(2)}\right), \\ \beta_1^{(2)} &= 4\left[J_1^{(2)} \cos(k_x a) + J_3^{(2)} \cos(k_z b)\right], \\ \alpha_2 &= 8J_2, \\ \beta_2 &= 4J_2\left[\cos\left(\tfrac{1}{2}k_x a + \tfrac{1}{2}k_z b\right) + \cos\left(\tfrac{1}{2}k_x a - \tfrac{1}{2}k_z b\right)\right]. \end{aligned} \tag{A3}$$

Here the superscript indicates the position of the local moment in the unit cell. The Hamiltonian for sublattice 2 is found by substitution of $1 \rightleftharpoons 2$. The solutions now include in- and out-of-phase intralayer excitations. We list the LL matrices in the presence an external field along the b and a axes below.

1. Ferromagnetic phase—Easy axis external field

The eigenvalue matrix in the basis of

$$\begin{bmatrix} m_x^{(1)} \\ m_x^{(2)} \\ m_y^{(1)} \\ m_y^{(2)}, \end{bmatrix} \tag{A4}$$

for an external field along the (positive) easy axis reads

$$\begin{bmatrix} 0 & 0 & iA^{(1)} & -iA_1 \\ 0 & 0 & -iA_1 & iA^{(2)} \\ -iB^{(1)} & iB_1 & 0 & 0 \\ iB_1 & -iB^{(2)} & 0 & 0 \end{bmatrix}, \tag{A5}$$

where

$$\begin{aligned} A^{(1)} &= B_0 + 2(D_z - D_y) + \left[\alpha_1^{(1)} - \beta_1^{(1)}\right] + \alpha_2 + \mu_0 M_s f(k), \\ A^{(2)} &= B_0 + 2(D_z - D_y) + \left[\alpha_1^{(2)} - \beta_1^{(2)}\right] + \alpha_2 + \mu_0 M_s f(k), \\ B^{(1)} &= B_0 + 2(D_z - D_x) + \left[\alpha_1^{(1)} - \beta_1^{(1)}\right] \\ &\quad + \alpha_2 + \frac{k_x^2}{k^2}\mu_0 M_s[1 - f(k)], \\ B^{(2)} &= B_0 + 2(D_z - D_x) + \left[\alpha_1^{(2)} - \beta_1^{(2)}\right] \\ &\quad + \alpha_2 + \frac{k_x^2}{k^2}\mu_0 M_s[1 - f(k)], \\ A_1 &= \beta_2 - \mu_0 M_s f(k), \\ B_1 &= \beta_2 - \frac{k_x^2}{k^2}\mu_0 M_s[1 - f(k)]. \end{aligned} \tag{A6}$$

2. Canted phase—Intermediate axis external field

The eigenvalue matrix for the canted and saturated ($\theta = \theta/2$) phases reads

$$\begin{bmatrix} 0 & 0 & iC^{(1)} & -iC_1 \\ 0 & 0 & -iC_1 & iC^{(2)} \\ -iD^{(1)} & iD_1 & 0 & 0 \\ iD_1 & -iD^{(2)} & 0 & 0 \end{bmatrix}, \tag{A7}$$

where

$$\begin{aligned} C^{(1)} &= B_0 \sin(\theta) + 2[D_x \sin^2(\theta) + D_z \cos^2(\theta) - D_y] \\ &\quad + \left[\alpha_1^{(1)} - \beta_1^{(1)}\right] + \alpha_2 + \mu_0 M_s f(k), \\ C^{(2)} &= B_0 \sin(\theta) + 2[D_x \sin^2(\theta) + D_z \cos^2(\theta) - D_y] \\ &\quad + \left[\alpha_1^{(2)} - \beta_1^{(2)}\right] + \alpha_2 + \mu_0 M_s f(k), \\ D^{(1)} &= B_0 \sin(\theta) + 2(D_z - D_x)\cos(2\theta) \\ &\quad + \left[\alpha_1^{(1)} - \beta_1^{(1)}\right] + \alpha_2 + \mu_0 M_s \frac{k_\alpha^2}{k^2}[1 - f(k)], \\ D^{(2)} &= B_0 \sin(\theta) + 2(D_z - D_x)\cos(2\theta) \\ &\quad + \left[\alpha_1^{(2)} - \beta_1^{(2)}\right] + \alpha_2 + \mu_0 M_s \frac{k_\alpha^2}{k^2}[1 - f(k)], \\ C_1 &= \beta_2 - \mu_0 M_s f(k), \\ D_1 &= \beta_2 - \mu_0 M_s \frac{k_\alpha^2}{k^2}[1 - f(k)]. \end{aligned} \tag{A8}$$

APPENDIX B: TWO-SUBLATTICE BILAYER CrSBr

The 8×8 LL matrix for the bilayer with anisotropic exchange interactions cannot be analytically diagonalized but the listed forms here can be easily solved numerically. The Hamiltonian of the bilayer is the sum of the separate monolayers with an interaction term which now has two contributions in the form of Eq. (4), one for each magnetic atom in the monolayer unit cell. The corresponding matrix forms of the LL equation for the AFM, FM, and canted phases are given below.

1. Antiferromagnetic and ferromagnetic phase

In the basis

$$\begin{bmatrix} m_{x,A}^{(1)} \\ m_{x,B}^{(1)} \\ m_{x,A}^{(2)} \\ m_{x,B}^{(2)} \\ m_{y,A}^{(1)} \\ m_{y,B}^{(1)} \\ m_{y,A}^{(2)} \\ m_{y,B}^{(2)} \end{bmatrix}, \tag{B1}$$

the dynamical LL matrix for the AFM phase reads

$$\begin{bmatrix} 0 & 0 & 0 & 0 & iE_1^{(1)} & -iJ_\perp & -iE & 0 \\ 0 & 0 & 0 & 0 & iJ_\perp & -iE_2^{(1)} & 0 & iE \\ 0 & 0 & 0 & 0 & -iE & 0 & iE_1^{(2)} & -iJ_\perp \\ 0 & 0 & 0 & 0 & 0 & iE & iJ_\perp & -iE_2^{(2)} \\ -iF_1^{(1)} & iJ_\perp & iF & 0 & 0 & 0 & 0 & 0 \\ -iJ_\perp & iF_2^{(1)} & 0 & -iF & 0 & 0 & 0 & 0 \\ iF & 0 & -iF_1^{(2)} & iJ_\perp & 0 & 0 & 0 & 0 \\ 0 & -iF & -iJ_\perp & iF_2^{(2)} & 0 & 0 & 0 & 0 \end{bmatrix}, \tag{B2}$$

where

$$\begin{aligned}
E_1^{(1)} &= B_0 + 2(D_z - D_y) + \left[\alpha_1^{(1)} - \beta_1^{(1)}\right] + \alpha_2 - J_\perp + \mu_0 M_s f(k), \\
E_1^{(2)} &= B_0 + 2(D_z - D_y) + \left[\alpha_1^{(2)} - \beta_1^{(2)}\right] + \alpha_2 - J_\perp + \mu_0 M_s f(k), \\
E_2^{(1)} &= -B_0 + 2(D_z - D_y) + \left[\alpha_1^{(1)} - \beta_1^{(1)}\right] + \alpha_2 - J_\perp + \mu_0 M_s f(k), \\
E_2^{(2)} &= -B_0 + 2(D_z - D_y) + \left[\alpha_1^{(2)} - \beta_1^{(2)}\right] + \alpha_2 - J_\perp + \mu_0 M_s f(k), \\
E &= \beta_2 - \mu_0 M_s f(k), \\
F_1^{(1)} &= B_0 + 2(D_z - D_x) + \left[\alpha_1^{(1)} - \beta_1^{(1)}\right] + \alpha_2 - J_\perp + \mu_0 M_s \frac{k_x^2}{k^2}[1 - f(k)], \\
F_1^{(2)} &= B_0 + 2(D_z - D_x) + \left[\alpha_1^{(2)} - \beta_1^{(2)}\right] + \alpha_2 - J_\perp + \mu_0 M_s \frac{k_x^2}{k^2}[1 - f(k)], \\
F_2^{(1)} &= -B_0 + 2(D_z - D_x) + \left[\alpha_1^{(1)} - \beta_1^{(1)}\right] + \alpha_2 - J_\perp + \mu_0 M_s \frac{k_x^2}{k^2}[1 - f(k)], \\
F_2^{(2)} &= -B_0 + 2(D_z - D_x) + \left[\alpha_1^{(2)} - \beta_1^{(2)}\right] + \alpha_2 - J_\perp + \mu_0 M_s \frac{k_x^2}{k^2}[1 - f(k)], \\
F &= \beta_2 - \mu_0 M_s \frac{k_x^2}{k^2}[1 - f(k)].
\end{aligned} \tag{B3}$$

For the FM phase, the LL matrix reads

$$\begin{bmatrix} 0 & 0 & 0 & 0 & iG^{(1)} & -iJ_\perp & -iG_1 & 0 \\ 0 & 0 & 0 & 0 & -iJ_\perp & iG^{(1)} & 0 & -iG_1 \\ 0 & 0 & 0 & 0 & -iG_1 & 0 & iG^{(2)} & -iJ_\perp \\ 0 & 0 & 0 & 0 & 0 & -iG_1 & -iJ_\perp & iG^{(2)} \\ -iH^{(1)} & iJ_\perp & iH_1 & 0 & 0 & 0 & 0 & 0 \\ iJ_\perp & -iH^{(1)} & 0 & iH_1 & 0 & 0 & 0 & 0 \\ iH_1 & 0 & -iH^{(2)} & iJ_\perp & 0 & 0 & 0 & 0 \\ 0 & iH_1 & iJ_\perp & -iH^{(2)} & 0 & 0 & 0 & 0 \end{bmatrix}, \tag{B4}$$

where

$$\begin{aligned} G^{(1)} &= B_0 + 2(D_z - D_y) + \left[\alpha_1^{(1)} - \beta_1^{(1)}\right] + \alpha_2 + J_\perp + \mu_0 M_s f(k), \\ G^{(2)} &= B_0 + 2(D_z - D_y) + \left[\alpha_1^{(2)} - \beta_1^{(2)}\right] + \alpha_2 + J_\perp + \mu_0 M_s f(k), \\ G_1 &= \beta_2 - \mu_0 M_s f(k), \\ H^{(1)} &= B_0 + 2(D_z - D_x) + \left[\alpha_1^{(1)} - \beta_1^{(1)}\right] + \alpha_2 + J_\perp + \mu_0 M_s \frac{k_x^2}{k^2}[1 - f(k)], \\ H^{(2)} &= B_0 + 2(D_z - D_x) + \left[\alpha_1^{(2)} - \beta_1^{(2)}\right] + \alpha_2 + J_\perp + \mu_0 M_s \frac{k_x^2}{k^2}[1 - f(k)], \\ H_1 &= \beta_2 - \mu_0 M_s \frac{k_x^2}{k^2}[1 - f(k)]. \end{aligned} \tag{B5}$$

2. Canted phase

When applying an external magnetic field along the intermediate axis, we expand the noncollinear phases in the basis

$$\begin{bmatrix} m_{\alpha,A}^{(1)} \\ m_{\alpha,B}^{(1)} \\ m_{\alpha,A}^{(2)} \\ m_{\alpha,B}^{(2)} \\ m_{\beta,A}^{(1)} \\ m_{\beta,B}^{(1)} \\ m_{\beta,A}^{(2)} \\ m_{\beta,B}^{(2)} \end{bmatrix}. \tag{B6}$$

For both canted and saturated ($\theta = \pi/2$) phases, the LL matrix reads

$$\begin{bmatrix} 0 & 0 & 0 & 0 & iI^{(1)} & -iJ_\perp & -iI_1 & 0 \\ 0 & 0 & 0 & 0 & -iJ_\perp & iI^{(1)} & 0 & -iI_1 \\ 0 & 0 & 0 & 0 & -iI_1 & 0 & iI^{(2)} & -iJ_\perp \\ 0 & 0 & 0 & 0 & 0 & -iI_1 & -iJ_\perp & iI^{(2)} \\ -iK_A^{(1)} & iK_2 & iK_{1,A} & 0 & 0 & 0 & 0 & 0 \\ iK_2 & -iK_B^{(1)} & 0 & iK_{1,B} & 0 & 0 & 0 & 0 \\ iK_{1,A} & 0 & -iK_A^{(2)} & iK_2 & 0 & 0 & 0 & 0 \\ 0 & iK_{1,B} & iK_2 & -iK_B^{(2)} & 0 & 0 & 0 & 0 \end{bmatrix}, \tag{B7}$$

where

$$\begin{aligned} I^{(1)} &= B_0 \sin(\theta) + 2[D_x \sin^2(\theta) + D_z \cos^2(\theta) - D_y] + \left[\alpha_1^{(1)} - \beta_1^{(1)}\right] + \alpha_2 - J_\perp \cos(2\theta) + \mu_0 M_s f(k), \\ I^{(2)} &= B_0 \sin(\theta) + 2[D_x \sin^2(\theta) + D_z \cos^2(\theta) - D_y] + \left[\alpha_1^{(2)} - \beta_1^{(2)}\right] + \alpha_2 - J_\perp \cos(2\theta) + \mu_0 M_s f(k), \\ I_1 &= \beta_2 - \mu_0 M_s f(k), \end{aligned}$$

$$
\begin{aligned}
K_A^{(1)} &= B_0 \sin(\theta) + 2(D_z - D_x)\cos(2\theta) + \left[\alpha_1^{(1)} - \beta_1^{(1)}\right] + \alpha_2 - J_\perp \cos(2\theta) + \mu_0 M_s \frac{k_{\alpha,A}^2}{k^2}[1 - f(k)],\\
K_B^{(1)} &= B_0 \sin(\theta) + 2(D_z - D_x)\cos(2\theta) + \left[\alpha_1^{(1)} - \beta_1^{(1)}\right] + \alpha_2 - J_\perp \cos(2\theta) + \mu_0 M_s \frac{k_{\alpha,B}^2}{k^2}[1 - f(k)],\\
K_A^{(2)} &= B_0 \sin(\theta) + 2(D_z - D_x)\cos(2\theta) + [\alpha_1^{(2)} - \beta_1^{(2)}] + \alpha_2 - J_\perp \cos(2\theta) + \mu_0 M_s \frac{k_{\alpha,A}^2}{k^2}[1 - f(k)],\\
K_B^{(2)} &= B_0 \sin(\theta) + 2(D_z - D_x)\cos(2\theta) + \left[\alpha_1^{(2)} - \beta_1^{(2)}\right] + \alpha_2 - J_\perp \cos(2\theta) + \mu_0 M_s \frac{k_{\alpha,B}^2}{k^2}[1 - f(k)],\\
K_{1,A} &= \beta_2 - \mu_0 M_s \frac{k_{\alpha,A}^2}{k^2}[1 - f(k)],\\
K_{1,B} &= \beta_2 - \mu_0 M_s \frac{k_{\alpha,B}^2}{k^2}[1 - f(k)],\\
K_2 &= -J_\perp \cos(2\theta).
\end{aligned}
\tag{B8}
$$

In the limit of isotropic interlayer exchanges $J_1^{(1)} = J_1^{(2)}$ and $J_3^{(1)} = J_3^{(2)}$, the solutions for a single atom per sublattice in the text correspond to the intralayer in-phase excitations, i.e.,

$$
\begin{aligned}
m_{\alpha,A}^{(1)} &= m_{\alpha,A}^{(2)},\\
m_{\beta,A}^{(1)} &= m_{\beta,A}^{(2)},\\
m_{\alpha,B}^{(1)} &= m_{\alpha,B}^{(2)},\\
m_{\beta,B}^{(1)} &= m_{\beta,B}^{(2)},
\end{aligned}
\tag{B9}
$$

but the dipolar field is twice as large by effective doubling of lattice sites. The intralayer out-of-phase excitations, or

$$
\begin{aligned}
m_{\alpha,A}^{(1)} &= -m_{\alpha,A}^{(2)},\\
m_{\beta,A}^{(1)} &= -m_{\beta,A}^{(2)},\\
m_{\alpha,B}^{(1)} e &= -m_{\alpha,B}^{(2)},\\
m_{\beta,B}^{(1)} &= -m_{\beta,B}^{(2)},
\end{aligned}
\tag{B10}
$$

correspond to the higher (optical) band folded back in the reduced Brillouin zone. The intralayer in-phase (out-of-phase) modes are characterized by parameter combinations $\alpha_i - \beta_i$ ($\alpha_i + \beta_i$) [13].

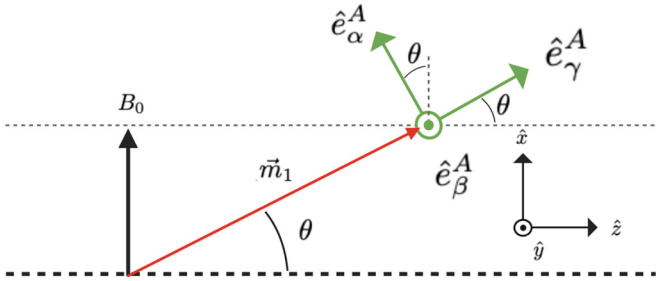

FIG. 5. Canted orientation of magnetic moments in the monolayer when $\vec{B}_{\rm Ext} \parallel \hat{x}$, including unit vectors in the rotated basis.

APPENDIX C: COORDINATE TRANSFORMATION AND BASE VECTORS FOR NONCOLLINEAR SPIN TEXTURES

In the following section, we describe the coordinate transformations that simplify the solution of the LL equation when the spin texture is noncollinear.

1. Monolayer—Canted phase

The canted phase in the monolayer is described in the basis of $[\hat{e}_\alpha^A, \hat{e}_\beta^A, \hat{e}_\gamma^A]$ with transformations

$$
\begin{aligned}
\hat{x} &= \cos(\theta)\hat{e}_\alpha^A + \sin(\theta)\hat{e}_\gamma^A,\\
\hat{y} &= \hat{e}_\beta^A,\\
\hat{z} &= -\sin(\theta)\hat{e}_\alpha^A + \cos(\theta)\hat{e}_\gamma^A,
\end{aligned}
\tag{C1}
$$

as illustrated in Fig. 5.

2. Bilayer—Canted phase

The canted phase in the bilayer is described in the bases of $[\hat{e}_\alpha^A, \hat{e}_\beta^A, \hat{e}_\gamma^A]$ and $[\hat{e}_\alpha^B, \hat{e}_\beta^B, \hat{e}_\gamma^B]$ with transformations

$$
\begin{aligned}
\hat{x} &= \cos(\theta)\hat{e}_\alpha^A + \sin(\theta)\hat{e}_\gamma^A,\\
\hat{y} &= \hat{e}_\beta^A,\\
\hat{z} &= -\sin(\theta)\hat{e}_\alpha^A + \cos(\theta)\hat{e}_\gamma^A,
\end{aligned}
\tag{C2}
$$

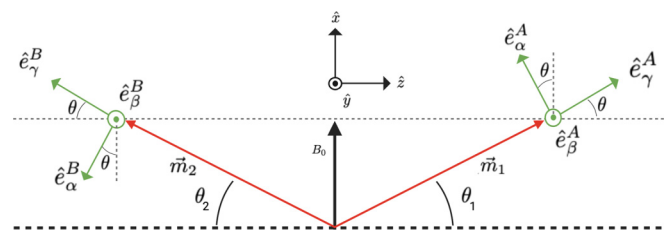

FIG. 6. Canted orientation of magnetic moments in the bilayer with $\vec{B}_{\rm Ext} \parallel \hat{x}$, including unit vectors in the noncollinear basis. A and B indicate magnetic moments in layers A and B, respectively.

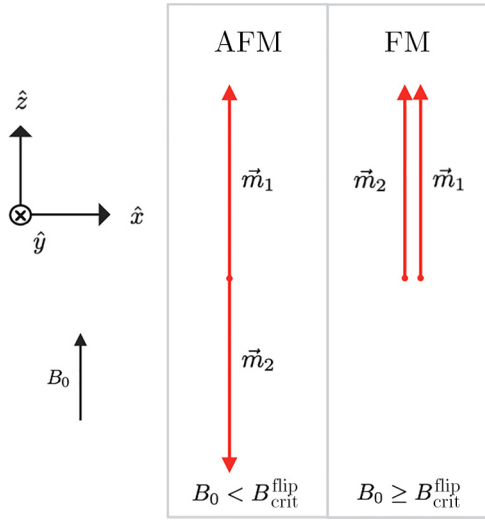

FIG. 7. Spin-flip phase transition in the bilayer.

and

$$\hat{x} = -\cos(\theta)\hat{e}_\alpha^B + \sin(\theta)\hat{e}_\gamma^B,$$
$$\hat{y} = \hat{e}_\beta^B,$$
$$\hat{z} = -\sin(\theta)\hat{e}_\alpha^B - \cos(\theta)\hat{e}_\gamma^B, \quad \text{(C3)}$$

as illustrated in Fig. 6.

APPENDIX D: BILAYER PHASE TRANSITIONS

In this section, we address the spin-flip and spin canting phase transitions illustrated.

1. Spin-flip transition

A "spin-flip" transition occurs at external fields $B_0 = B_{\rm flip}^{\rm crit}$ along the easy axis (z) as illustrated in Fig. 7. It should not be confused with the spin-flop transition in materials with stronger interlayer exchange coupling.

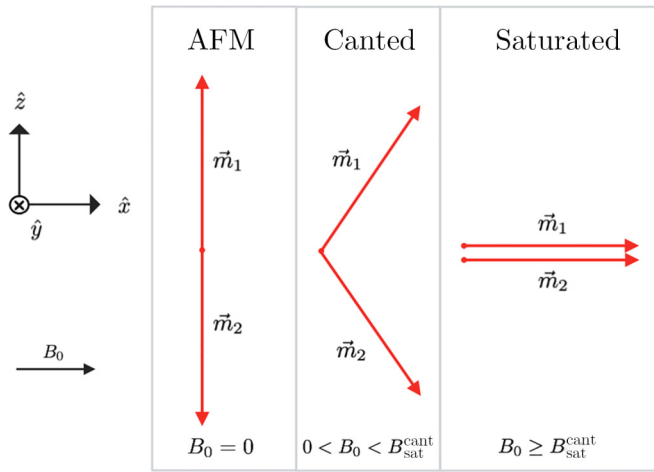

FIG. 8. Canted phase transition in the bilayer.

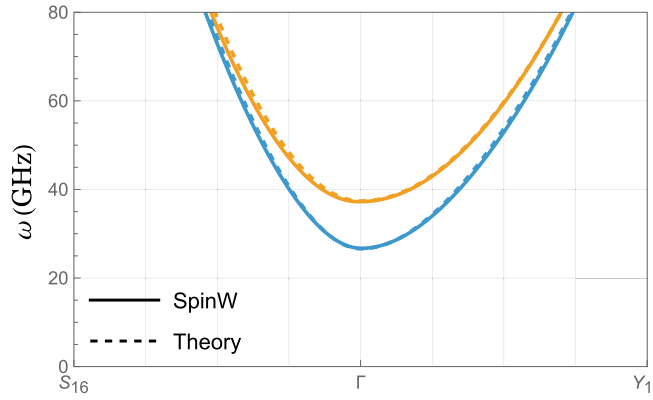

FIG. 9. Spin-wave dispersion of the bilayer in the AFM phase computed by the simulation package SPINW (solid curve) and our model (dashed lines).

2. Canted phase transition

The continuous canting transition occurs for external fields oriented along the intermediate axis (x) in the bilayer (monolayer) for any field $B < B_0 < B_{\rm sat}^{\rm cant}$ $(0 < B_0 < B_{\rm sat})$. The magnetic moments are parallel to the intermediate axis for higher fields as illustrated in Fig. 8.

APPENDIX E: NUMERICAL VERIFICATION

Here we compare our model with numerical simulations using the program package SPINW [47]. Figure 9 shows the simulations (solid curve) and our analytical results (dashed lines) for the spin-wave dispersion in the AFM phase of the bilayer without an applied magnetic field [see solid curve in Fig. 3(c)].

Figure 10 shows the difference between results to be less than 3%.

The small discrepancies are caused on one hand by the truncation of dipolar interactions in SPINW at a user-specified distance that is limited by the available computer memory. On the other hand, they may be caused by the small interlayer dipolar interactions [39] that we disregard here.

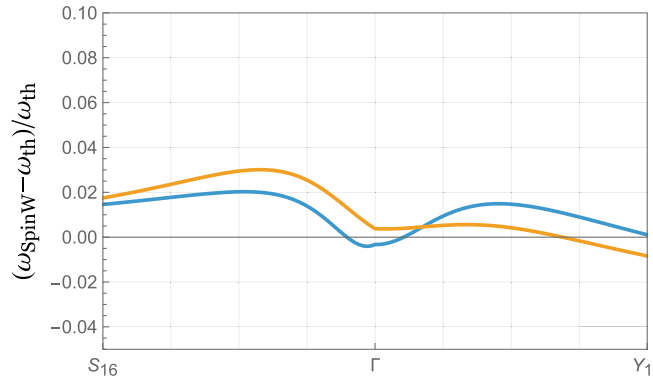

FIG. 10. Relative difference between the model and numerical simulations in Fig. 9.

[1] B. Huang, G. Clark, E. Navarro-Moratalla, D. R. Klein, R. Cheng, K. L. Seyler, D. Zhong, E. Schmidgall, M. A. McGuire, D. H. Cobden, W. Yao, D. Xiao, P. Jarillo-Herrero, and X. Xu, Layer-dependent ferromagnetism in a van der Waals crystal down to the monolayer limit, Nature (London) **546**, 270 (2017).

[2] C. Gong, L. Li, Z. Li, H. Ji, A. Stern, Y. Xia, T. Cao, W. Bao, C. Wang, Y. Wang, Z. Qiu, R. Cava, S. Louie, J. Xia, and X. Zhang, Discovery of intrinsic ferromagnetism in 2D van der Waals crystals, Nature (London) **546**, 265 (2017).

[3] A. Chumak, V. Vasyuchka, A. Serga, and B. Hillebrands, Magnon spintronics, Nat. Phys. **11**, 453 (2015).

[4] A. Mahmoud, F. Ciubotaru, F. Vanderveken, A. Chumak, S. Hamdioui, C. Adelmann, and S. Cotofana, Introduction to spin wave computing, J. Appl. Phys. **128**, 161101 (2020).

[5] Y. Deng, Y. Yu, Y. Song, J. Zhang, N. Wang, Y. Wu, J. Zhu, J. Wang, X. Chen, and Y. Zhang, Gate-tunable room-temperature ferromagnetism in two-dimensional Fe_3GeTe_2, Nature (London) **563**, 94 (2018).

[6] M. Bonilla, S. Kolekar, Y. Ma, H. Coy Diaz, V. Sankar, R. Das, T. Eggers, H. Rodriguez Gutierrez, M.-H. Phan, and M. Batzill, Strong room-temperature ferromagnetism in VSe_2 monolayers on van der Waals substrates, Nat. Nanotechnol. **13**, 289 (2018).

[7] S. Zhang, R. Xu, N. Luo, and X. Zou, Two-dimensional magnetic materials: Structures, properties and external controls, Nanoscale **13**, 1398 (2021).

[8] M. Gibertini, M. Koperski, A. Morpurgo, and K. Novoselov, Magnetic 2D materials and heterostructures, Nat. Nanotechnol. **14**, 408 (2019).

[9] B. Huang, G. Clark, D. Klein, D. MacNeill, E. Navarro-Moratalla, K. Seyler, N. Wilson, M. McGuire, D. Cobden, D. Xiao, W. Yao, P. Jarillo-Herrero, and X. Xu, Electrical control of 2D magnetism in bilayer CrI_3, Nat. Nanotechnol. **13**, 544 (2018).

[10] S. Jiang, J. Shan, and K. Mak, Electric-field switching of two-dimensional van der Waals magnets, Nat. Mater. **17**, 406 (2018).

[11] T. Li, S. Jiang, N. Sivadas, Z. Wang, Y. Xu, D. Weber, J. Goldberger, K. Watanabe, T. Taniguchi, C. Fennie, K. Mak, and J. Shan, Pressure-controlled interlayer magnetism in atomically thin CrI_3, Nat. Mater. **18**, 1303 (2019).

[12] Z. Lin, M. Lohmann, Z. A. Ali, C. Tang, J. Li, W. Xing, J. Zhong, S. Jia, W. Han, S. Coh, W. Beyermann, and J. Shi, Pressure-induced spin reorientation transition in layered ferromagnetic insulator $Cr_2Ge_2Te_6$, Phys. Rev. Mater. **2**, 051004(R) (2018).

[13] D. Esteras, A. Rybakov, A. Ruiz, and J. J. Baldoví, Magnon straintronics in the 2D van der Waals ferromagnet CrSBr from first-principles, Nano Lett. **22**, 8771 (2022).

[14] M. Šiškins, M. Lee, S. Mañas-Valero, E. Coronado, Y. Blanter, H. van der Zant, and P. Steeneken, Magnetic and electronic phase transitions probed by nanomechanical resonators, Nat. Commun. **11**, 2698 (2020).

[15] R. Roy Chowdhury, C. Patra, S. DuttaGupta, S. Satheesh, S. Dan, S. Fukami, and R. P. Singh, Modification of unconventional Hall effect with doping at the nonmagnetic site in a two-dimensional van der Waals ferromagnet, Phys. Rev. Mater. **6**, 014002 (2022).

[16] L. Lin, Q. Zhou, Y. Li, S. Yuan, Q. Chen, S. Dong, and J. Wang, Surface vacancy-induced switchable electric polarization and enhanced ferromagnetism in monolayer metal trihalides, Nano Lett. **18**, 2943 (2018).

[17] Y. Guo, Y. Zhang, S. Yuan, B. Wang, and J. Wang, Chromium sulfide halide monolayers: Intrinsic ferromagnetic semiconductors with large spin polarization and high carrier mobility, Nanoscale **10**, 18036 (2018).

[18] M. Ziebel, M. Feuer, J. Cox, X. Zhu, C. Dean, and X. Roy, CrSBr: An air-stable, two-dimensional magnetic semiconductor, Nano Lett. **24**, 4319 (2024).

[19] R. Duine, K.-J. Lee, S. Parkin, and M. Stiles, Synthetic antiferromagnetic spintronics, Nat. Phys. **14**, 217 (2018).

[20] C. Gong and X. Zhang, Two-dimensional magnetic crystals and emergent heterostructure devices, Science **363**, eaav4450 (2019).

[21] Z. Jiang, P. Wang, J. Xing, X. Jiang, and J. Zhao, Screening and design of novel 2D ferromagnetic materials with high Curie temperature above room temperature, ACS Appl. Mater. Interfaces **10**, 39032 (2018).

[22] K. Yang, G. Wang, L. Liu, D. Lu, and H. Wu, Triaxial magnetic anisotropy in the two-dimensional ferromagnetic semiconductor CrSBr, Phys. Rev. B **104**, 144416 (2021).

[23] C. W. Cho, A. Pawbake, N. Aubergier, A. L. Barra, K. Mosina, Z. Sofer, M. E. Zhitomirsky, C. Faugeras, and B. A. Piot, Microscopic parameters of the van der Waals CrSBr antiferromagnet from microwave absorption experiments, Phys. Rev. B **107**, 094403 (2023).

[24] T. Cham, S. Karimeddiny, A. Dismukes, X. Roy, D. Ralph, and Y. K. Luo, Anisotropic gigahertz antiferromagnetic resonances of the easy-axis van der Waals antiferromagnet CrSBr, Nano Lett. **22**, 6716 (2022).

[25] Y. Sun, F. Meng, C. Lee, A. Soll, H. Zhang, R. Ramesh, J. Yao, Z. Sofer, and J. Orenstein, Dipolar spin wave packet transport in a van der Waals antiferromagnet, Nat. Phys. **20**, 794 (2024).

[26] Z. Guo, H. Jiang, L. Jin, X. Zhang, Y. Liu, and X. Wang, Second-order topological insulator in ferromagnetic monolayer and antiferromagnetic bilayer CrSBr, Small Sci. **4**, 2300356 (2024).

[27] A. Scheie, M. Ziebel, D. Chica, Y. Bae, X. Wang, A. Kolesnikov, X. Zhu, and X. Roy, Spin waves and magnetic exchange Hamiltonian in CrSBr, Adv. Sci. **9**, 2202467 (2022).

[28] K. Lee, A. H. Dismukes, E. J. Telford, R. A. Wiscons, J. Wang, X. Xu, C. P. Nuckolls, C. R. Dean, X. Roy, and X. Zhu, Magnetic order and symmetry in the 2D semiconductor CrSBr, Nano Lett. **21**, 3511 (2020).

[29] F. Moro, S. Ke, A. Aguila, A. Söll, Z. Sofer, Q. Wu, M. Yue, L. Li, X. Liu, and M. Fanciulli, Revealing 2D magnetism in a bulk CrSBr single crystal by electron spin resonance, Adv. Funct. Mater. **32**, 2207044 (2022).

[30] A. Rudenko, M. Rösner, and M. Katsnelson, Dielectric tunability of magnetic properties in orthorhombic ferromagnetic monolayer CrSBr, npj Comput. Mater. **9**, 83 (2023).

[31] B. Wang, Y. Wu, Y. Bai, P. Shi, G. Zhang, Y. Zhang, and C. Liu, Origin and regulation of triaxial magnetic anisotropy in the ferromagnetic semiconductor CrSBr monolayer, Nanoscale **15**, 13402 (2023).

[32] C. Boix-Constant, S. Jenkins, R. Rama-Eiroa, E. J. G. Santos, S. Mañas-Valero, and E. Coronado, Multistep magnetization switching in orthogonally twisted ferromagnetic monolayers, Nat. Mater. **23**, 212 (2023).

[33] T. Ghiasi, M. Borst, S. Kurdi, B. Simon, I. Bertelli, C. Boix-Constant, S. Mañas-Valero, H. van der Zant, and T. van der

Sar, Nitrogen-vacancy magnetometry of CrSBr by diamond membrane transfer, npj 2D Mater. Appl. **7**, 62 (2023).
[34] S. Rezende, A. Azevedo, and R. Rodríguez-Suárez, Introduction to antiferromagnetic magnons, J. Appl. Phys. **126**, 151101 (2019).
[35] B. Hillebrands, Spin-wave calculations for multilayered structures, Phys. Rev. B **41**, 530 (1990).
[36] J. Jiménez-Bustamante, N. Vidal-Silva, A. Kákay, S. Wintz, and R. Gallardo, Impact of layer count and thickness on spin wave modes in multilayer synthetic antiferromagnets, Sci. Rep. **15**, 21545 (2025).
[37] D. Stancil and A. Prabhakar, *Spin Waves: Theory and Applications* (Springer, Berlin, 2009).
[38] R. L. Stamps, Spin configurations and spin-wave excitations in exchange-coupled bilayers, Phys. Rev. B **49**, 339 (1994).
[39] R. den Teuling, R. Das, A. V. Bondarenko, G. E. W. Bauer, Y. M. Blanter, and E. V. Tartakovskaya, Dipolar-exchange spin waves in thin bilayers, Low Temp. Phys. **51**, 998 (2025).
[40] R. Verba, G. Melkov, V. Tiberkevich, and A. Slavin, Collective spin-wave excitations in a two-dimensional array of coupled magnetic nanodots, Phys. Rev. B **85**, 014427 (2012).
[41] E. V. Tartakovskaya, M. Pardavi-Horvath, and R. D. McMichael, Spin-wave localization in tangentially magnetized films, Phys. Rev. B **93**, 214436 (2016).
[42] J. Harms and R. Duine, Theory of the dipole-exchange spin wave spectrum in ferromagnetic films with in-plane magnetization revisited, J. Magn. Magn. Mater. **557**, 169426 (2022).
[43] M. Watson, S. Acharya, J. Nunn, L. Nagireddy, D. Pashov, M. Rösner, M. Schilfgaarde, N. Wilson, and C. Cacho, Giant exchange splitting in the electronic structure of A-type 2D antiferromagnet CrSBr check for updates, npj 2D Mater. Appl. **8**, 54 (2024).
[44] F. B. Anderson and H. B. Callen, Statistical mechanics and field-induced phase transitions of the Heisenberg antiferromagnet, Phys. Rev. **136**, A1068 (1964).
[45] C. Kittel, Theory of antiferromagnetic resonance, Phys. Rev. **82**, 565 (1951).
[46] J. Gückelhorn, A. Kamra, T. Wimmer, M. Opel, S. Geprägs, R. Gross, H. Huebl, and M. Althammer, Influence of low-energy magnons on magnon Hanle experiments in easy-plane antiferromagnets, Phys. Rev. B **105**, 094440 (2022).
[47] S. Toth and B. Lake, Linear spin wave theory for single-Q incommensurate magnetic structures, J. Phys.: Condens. Matter **27**, 166002 (2015).
[48] L. Ortmanns, G. Bauer, and Y. Blanter, Magnon dispersion in bilayers of two-dimensional ferromagnets, Phys. Rev. B **103**, 155430 (2021).
[49] R. den Teuling, R. Das, A. V. Bondarenko, E. V. Tartakovskaya, G. E. W. Bauer, and Y. M. Blanter, Dataset for "Spin waves in the bilayer van der Waals magnet CrSBr," figshare (2025), https://doi.org/10.6084/m9.figshare.30075193.v1.

Correction: In Eq. (30), each occurrence of E has been changed to K_1.